Provided for non-commercial research and education use.
Not for reproduction, distribution or commercial use.

This article appeared in a journal published by Elsevier. The attached copy is furnished to the author for internal non-commercial research and education use, including for instruction at the authors institution and sharing with colleagues.

Other uses, including reproduction and distribution, or selling or licensing copies, or posting to personal, institutional or third party websites are prohibited.

In most cases authors are permitted to post their version of the article (e.g. in Word or Tex form) to their personal website or institutional repository. Authors requiring further information regarding Elsevier's archiving and manuscript policies are encouraged to visit:

http://www.elsevier.com/copyright

Author's personal copy

Planetary and Space Science 61 (2012) 60–65

Contents lists available at ScienceDirect

Planetary and Space Science

journal homepage: www.elsevier.com/locate/pss

Energetic charged particle weathering of Saturn's inner satellites

C. Paranicas [a,*], E. Roussos [b], N. Krupp [b], P. Kollmann [b], A.R. Hendrix [c], T. Cassidy [c], R.E. Johnson [d], P. Schenk [e], G. Jones [f], J. Carbary [a], D.G. Mitchell [a], K. Dialynas [g]

[a] APL, 11100 Johns Hopkins Rd., Laurel, MD 20723, USA
[b] MPS, Max-Planck-Str. 2, 37191 Katlenburg-Lindau, Germany
[c] Jet Propulsion Lab, 4800 Oak Grove Dr., Pasadena, CA 91109, USA
[d] UVA, Thornton Hall B102, Charlottesville, VA 22904, USA
[e] LPI, 3600 Bay Area Blvd., Houston, TX 77058, USA
[f] MSSL, UCL, Surrey RH5 6NT, United Kingdom
[g] University of Athens, Athens, Greece

ARTICLE INFO

Article history:
Received 30 November 2010
Received in revised form
11 February 2011
Accepted 21 February 2011
Available online 12 March 2011

Keywords:
Planetary magnetospheres
Saturn
Planetary satellites

ABSTRACT

We characterize the relative importance of energetic electrons and protons to the weathering of five of the inner satellites of Saturn. To do this, we present data from the Magnetospheric Imaging Instrument on the Cassini spacecraft, some of which is averaged over the whole mission to date. We also compute averaged proton and electron energy spectra relevant to the distances of these inner satellites. Where data are available, we estimate the power per unit area into a satellite's surface. For electron energy deposition into satellite leading hemispheres, we find the power per unit area is greatest at Mimas and falls off with distance from Saturn. Using fluxes of 1–50 MeV protons detected within the sweeping corridors of Mimas and Enceladus, we find the corresponding deposition would be about 2×10^8 and 3.7×10^7 eV/cm^2 s.

© 2011 Elsevier Ltd. All rights reserved.

1. Introduction

A number of physical and chemical modifications of icy surfaces in space have been attributed to weathering by charged particles. In some cases, laboratory studies exist to provide a basis for connecting weathering agents with expected effects. However, the applicability of such studies to surfaces in space has limitations because of simultaneous weathering by different particle species over broad energy ranges. For this reason, we believe that an empirical approach to correlate particle bombardment patterns with optical features is warranted. In this paper, we present energetic charged particle data obtained near five of the inner satellites of Saturn and illustrate major differences in the weathering environments of these moons.

The importance of charged particles in surface modifications has been described in the literature for several decades (see, Johnson, 1990 and references therein). Recent examples in Solar System contexts support the importance of charged particle weathering in modifying the optical surface. For example, Khurana et al. (2007) have explained the so-called bright polar cap feature of Ganymede (e.g., Johnson, 1985) by mapping the edge of the bright region to the open/closed field line boundary of the internally generated magnetic field of that moon. Open and closed Ganymede field lines have been observed to have different levels of charged particle flux (Williams et al., 1998). Khurana's work provided some of the most compelling evidence to date of the role of charged particles in modifying surfaces. Other studies have noted pronounced leading versus trailing hemisphere differences in the abundances of trace atoms and molecules identified spectrally in the surface (e.g., Johnson et al., 2004; Carlson et al., 2009). Leading–trailing asymmetries in albedo are also present (e.g., McEwen, 1986; Buratti et al., 1998). Candidate weathering agents that exhibit such differences are charged and neutral particles, and dust.

Among charged particles, there are distinct energy ranges that are important for weathering. These can be loosely termed the cold plasma, ring-current particles, and radiation belt particles, following Schulz and Lanzerotti (1974). Schulz and Lanzerotti (1974) distinguished the ring-current energy range from the radiation belt energies by the relative importance of the corotation electric field on the particle's motion. In Saturn's inner magnetosphere, electrons with energies above approximately one to a few MeV (depending on L shell and pitch angle) have their net guiding center motion in the direction opposite to the plasma flow. This means that they are moving opposite to the direction dictated by the corotation electric field and for our purposes may be considered radiation belt particles. For protons in the few MeV energy range, the corotation drift is a fraction of the gradient-curvature drift and in the same direction.

* Corresponding author: Tel.: +1 240 228 8652; fax: +1 240 288 0386.
E-mail address: chris.paranicas@jhuapl.edu (C. Paranicas).

0032-0633/$ - see front matter © 2011 Elsevier Ltd. All rights reserved.
doi:10.1016/j.pss.2011.02.012

Author's personal copy

While the cold plasma flows onto all the inner satellites, the differences in the two other populations from the point of view of weathering are very dramatic. Tethys ($r=4.89R_S$) is approximately at the outer boundary of the most intense radiation belts, whereas Enceladus ($r=3.95R_S$) is near the inner boundary of the injected ring-current particles.

In this paper, we will focus on data from Cassini's Magnetosphere Imaging Instrument (MIMI) described by Krimigis et al. (2004). We mostly use data from the Low Energy Magnetospheric Measurement System (LEMMS) and the Ion and Neutral Camera (INCA). Together these sensors can detect charged particles from a few keV to tens of MeV in energy.

2. Distribution of energetic electrons

The radiation belts of Saturn are much less intense than those of Earth, Jupiter or Uranus (Mauk and Fox, 2010). In Fig. 1, we show data from the Cassini LEMMS sensor obtained between mid-2004 and mid-2010. These data are average intensities of 0.79–4.75 MeV electrons. The large spatial bins and the wide energy channel passband obscure some structure in physical space and in energy. But this plot does illustrate that the approximately MeV electron fluxes decrease by several orders of magnitude between the orbits of Mimas and Rhea. Below this energy, the distribution of energetic electrons by radial distance varies dramatically (Carbary et al., 2009; Kollmann et al., in press). We will discuss this further below.

At Saturn, the gradient-curvature drift of energetic electrons is opposite to the direction of the cold plasma flow. As noted above, the guiding centers of very energetic electrons can have net longitudinal motion that is retrograde. With respect to the satellites, the prograde versus retrograde transition energies for electrons with mirror latitudes of 15° (equatorial pitch angles of about 59°) are 1.12 MeV (Mimas and Enceladus), 1.01 MeV (Tethys), 0.835 MeV (Dione), and 0.612 MeV (Rhea). Thomsen and Van Allen (1980) call these transitions "resonant energies." Electrons at these energies can diffuse radially through the moon's orbit and avoid absorption. Below the resonant energies, electrons encounter the satellite first along the trailing hemisphere whereas above it they first encounter the satellite along its leading hemisphere.

To quantify the differences in leading hemisphere weathering by energetic electrons at the different satellites, we show energy spectra in Fig. 2 corresponding to the distances of the five main inner satellites. These values are obtained from median-average fluxes obtained by binning data from the LEMMS sensor on Cassini. Any time the spacecraft visited the spatial region represented by the bin, between mid-2004 and mid-2010, the data were included in the average. Here we have selected five electron channels from LEMMS based on various factors. These factors include properties of the energy passband and the level of background counts we expect the channel to receive in the radiation belt region. Even with these restrictions, the intensities corresponding to 50 and 75 keV have some contributions from electrons that are not in the nominal passband of the channel.

At the low energies, the highest fluxes correspond to the largest distances from the planet; this is likely due to the presence of injections and will be discussed in more detail below. Above about 1 MeV, the intensities are fairly well organized from the highest to the lowest with increasing distance from the planet. It is useful to note that at about 2 MeV, the intensities are an order of magnitude lower at Dione than Tethys. Furthermore, at approximately the MeV energy range, the spectrum steepens near the outer satellites. A way to understand this is that the radiation belt flux is below the instrument's background levels at Dione's position (Fig. 1).

We previously connected leading hemisphere weathering by energetic electrons with optical features on Mimas and Tethys (Schenk et al., 2011). We argued in that paper that equatorial latitudes on satellite leading hemispheres would be heavily weathered by MeV electrons. This can be appreciated by considering the following. Among retrograde electrons at a satellite's orbit, those with the highest number are near the drift resonance in a falling energy spectrum. Such electrons have very slow motion in the longitudinal direction relative to the satellite. At the same time, their bounce motion is very fast. These electrons therefore precipitate as soon as their guiding-center field line comes into contact with the satellite. This occurs near the leading hemisphere equator. We note further that E ring grains preferentially impact Mimas's trailing hemisphere and Tethys's leading hemisphere (Hamilton and Burns, 1994). Therefore, unlike dust and lower energy charged particles, energetic electrons are the only weathering agents that deposit significant amounts of energy on the leading hemispheres of both Mimas and Tethys. A lens-shaped feature appears in visible images of the leading hemispheres of these moons and is likely the result of the interaction of energetic electrons with the icy surfaces (Schenk et al., 2011).

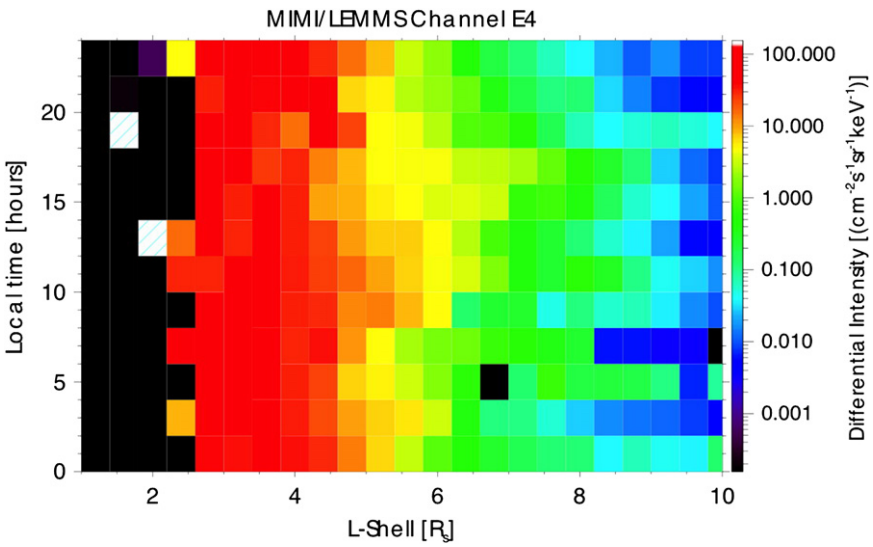

Fig. 1. Intensity map of 0.79–4.75 MeV electrons as a function of dipole L shell and local time. Fluxes obtained between mid-2004 and mid-2010 have been averaged and binned.

Author's personal copy

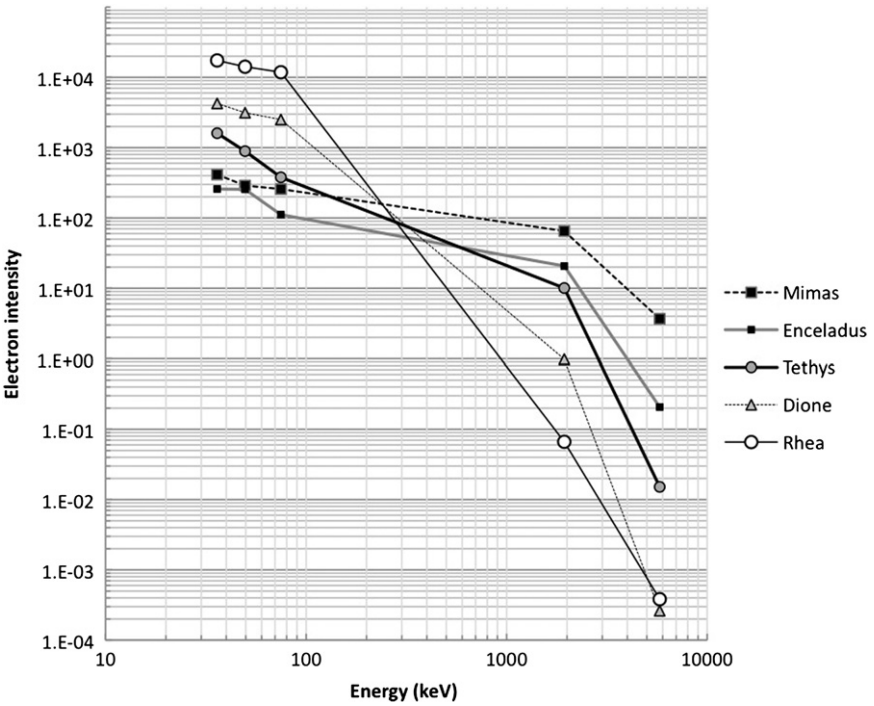

Fig. 2. Differential energy spectra (electrons per cm^2 s sr keV) at the L shells of the five inner satellites of Saturn. The fluxes represent background-corrected data averaged from mid-2004 to mid-2010.

As Fig. 2 illustrates, the ring-current electrons have completely different behavior from the radiation belt ones. Tens to hundreds of keV electrons are likely supplied to small Saturn radial distances by rapid injections. A possible scenario for creating these electrons is that they are first heated by the induced electric field associated with dipolarization. These electrons are then further energized by inward transport and conservation of adiabatic invariants of motion. Both Carbary et al. (2009) and Paranicas et al. (2010) presented summary plots of tens to hundreds of keV electrons in Saturn's magnetosphere. Both studies found decreasing intensity of these electrons inward of about Rhea's orbit (see, also, Kollmann et al., in press). Both also revealed strong local-time asymmetries, with much higher fluxes near midnight. Higher intensity near midnight is consistent with the spacecraft encountering more large-scale injections at that local time.

The data in Fig. 2 show that the lower energy fluxes are organized with the highest intensity at the largest distance (opposite to the radiation belt energies). The decrease of intensity with decreasing radial distance may be due to the fact that the inward motion of injected electrons is inhibited by the stronger dipole field of the inner magnetosphere. Furthermore, the region inward of about Enceladus's orbit is not strongly populated by direct injections (see, Paranicas et al., 2010). Loss rates are a factor as well; once electrons are injected deep into the magnetosphere, they are cooled and scattered in the environment dominated by dense neutral gas and grains.

3. Distribution of energetic protons

For the region of interest to us here, the above separation into three energy ranges is also very useful for ions. This is because the neutral gas in Saturn's inner magnetosphere has a much larger effect on charged particles with ring-current energies. For example, protons below about 200 keV and singly charged oxygen ions up to MeV energies undergo charge-exchange (CE) with neutrals (e.g., McEntire and Mitchell, 1989) and are lost as energetic neutral atoms (ENAs). In these collisions, the energetic ion is effectively replaced by a lower energy ion. In charge exchange at lower energies, there is no net loss of plasma ions because these collisions begin and end with one ion. Radiation belt protons survive longer than lower energy ions because their CE cross-sections with neutrals are typically very low.

The ionic radiation belts of Saturn are characterized by a several-order-of-magnitude increase in particle intensity from cosmic-ray background levels to peak levels (e.g., Krupp et al., 2009). Roussos et al. (2008) demonstrated that MeV ion absorption at Tethys isolates the inner belts ($L<5$) from the middle and outer magnetosphere. Armstrong et al. (2009) found much higher fluxes of protons in the radiation belts than other ions. For ions whose source is CRAND (cosmic ray albedo neutron decay, see, for instance, Cooper, 1983), this is expected because it involves neutron decay. Roussos et al. (2011) have examined ways to populate the radiation belts in other ions to explain the data.

Below this energy in the ring-current range, the inner magnetosphere appears to be injection dominated (Paranicas et al., 2008). For a portion of the energy spectrum for each ion, there are very low steady-state fluxes with higher fluxes associated with recent injections. To illustrate this, we show an ENA image of Saturn's inner magnetosphere taken from high latitude in Fig. 3. This figure combines about 13 h of 55–90 keV neutral hydrogen data projected onto the equatorial plane of Saturn. This figure has been corrected for the Compton–Getting effect as it applies to ENAs.

It is noteworthy that the dominant ENA signal shown in Fig. 3 is near the orbit of Rhea. Carbary et al. (2008) surveyed the injected ion populations that create these ENAs in the Cassini INCA data. They found that large-scale injected ion populations tend to have their peak emission at about Rhea's orbit with some injected populations reaching inward of that distance. The nearly absent emission from inward of about Dione's orbit, where we know the neutral densities are high, means these ion fluxes are drastically reduced in a steady-state sense at these distances.

To quantify the effects of the neutral gas on energetic ions, we next turn to energy spectra. Dialynas et al. (2009) have shown

Author's personal copy

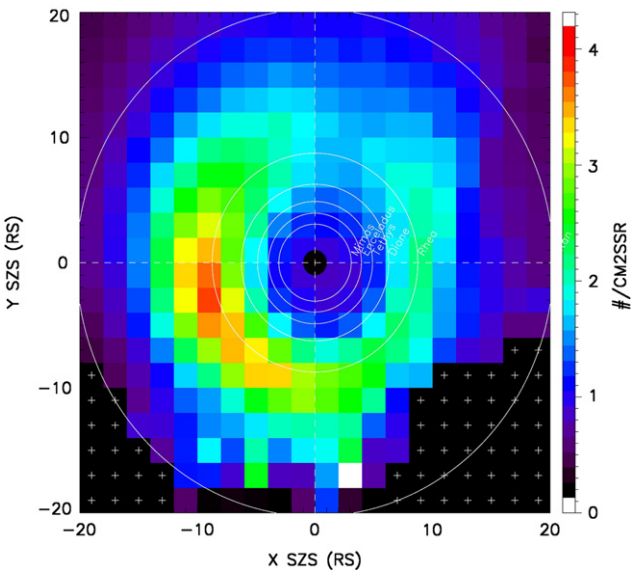

Fig. 3. Intensity map of energetic neutral hydrogen (55–90 keV) obtained on days 49–50 during 2007 using the INCA sensor. The data have been projected onto the equatorial plane and corrected for the Compton–Getting effect. The *x*-axis points sunward, while the *y*-axis points towards dusk.

proton and oxygen spectra during a few separate time periods. Here, we have averaged LEMMS data from about mid-2004 to mid-2010, excluding times of transient radiation belts (Roussos et al., 2008). In Fig. 4, we show proton energy spectra near the five inner satellites of interest. The data are logarithmic averages using all local pitch angles. We have excluded points where background counts were a concern. Also, some channels are pure proton channels while others are total ion channels that we believe are dominated by protons. For the two inner satellites, we use a narrow radial range corresponding to fluxes inside the sweeping corridor to create the spectra. The intensity peak in Fig. 4 in the tens of MeV energy range, most prominent at Mimas, is due to CRAND.

Regarding weathering, these particles would produce features with patterns similar to those produced by the electron spectra presented in the previous section. That is, at the highest energies corresponding to radiation belt particles, the highest fluxes are near the innermost moons. At low energies there are higher fluxes at Rhea than Tethys or Dione, because the principal source of injections is outside Rhea's orbit and also because Rhea is outside the densest part of the gas cloud.

4. Discussion

In this section we discuss the relative effects of charged particle weathering on the inner satellites. Cold plasma will flow first onto a satellite's trailing hemisphere as it overtakes the moon in its orbit. This tends to give a bull's-eye pattern to the bombardment that is centered on the trailing hemisphere apex. At higher energies, the pattern departs from this simple geometry. For example, Pospieszalska and Johnson (1989) showed how the bombardment pattern changes between the eV and the keV energy range on Dione. A crude way to estimate the energetic particle pattern onto an inert body is to compare the time for a charged particle to move up a field line and be reflected back (the half bounce time) with the time it takes the particle's guiding center to move a distance of about the moon's diameter in the longitudinal direction, as we showed at Europa earlier (Paranicas et al., 2001). For electrons, the bounce time is typically shorter than the net drift time across the body and hemispherical asymmetries in the bombardment pattern

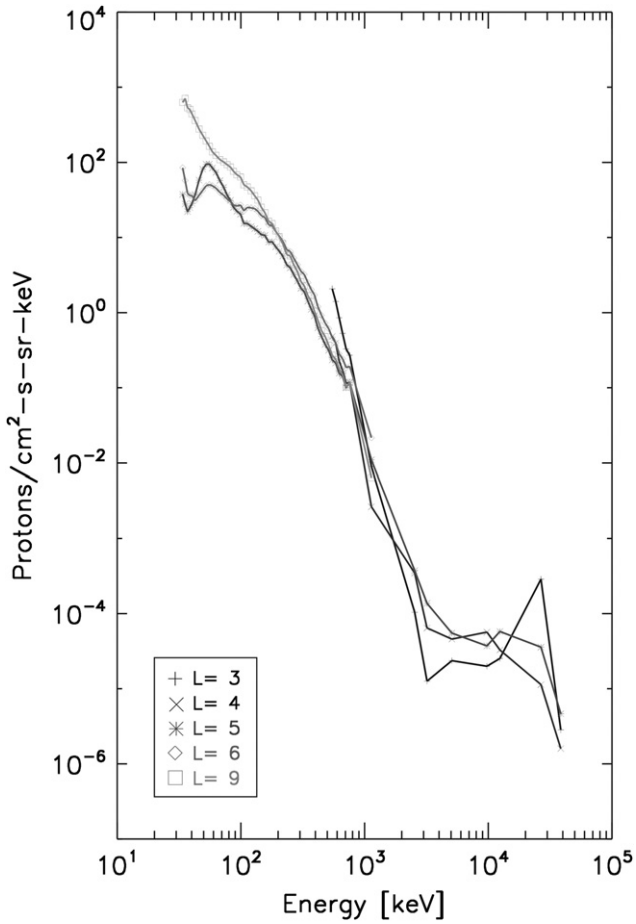

Fig. 4. Background-subtracted proton energy spectra near the five main inner satellites of Saturn. These data are averaged over the time period from mid-2004 to mid-2010. The LEMMS total ion and proton channels are used. The data were binned in Saturn radii as follows: 3.08 ± 0.01, 3.95 ± 0.01, 5 ± 0.5, 6 ± 0.5, and 9 ± 0.5.

are predicted. As noted above, there is also a shift from preferentially trailing to preferentially leading bombardment when electrons above about 1 MeV are considered. More refined descriptions of the morphology of the plasma effects on these bodies that include, for instance, corrections due to the ratio of the gyroradius to the moon radius and flow diversion around the moon are being considered.

When particles have access to a moon's surface, the energy per unit time deposited into the ice gives a measure of the steady-state effect. The net integrated isotropic flux across a surface in space is, $\pi \int j(E)dE$ (e.g., Sullivan, 1971). If each particle carries an energy E, then the energy flux deposited into the surface is

$$P = \pi \int jE\,dE \tag{1}$$

To perform this integral, we fit the electron energy spectra in Fig. 2 with the function,

$$j = j_o E^a \left(1 + \left(\frac{E}{E_o}\right)\right)^b \tag{2}$$

We present the fit parameters in Table 1 near the five satellites. Since there is a lot of variation at the low energies from injections, we tailor the fits to roughly approximate the data at low energy and closely fit the power law at high energy. We have calculated a goodness of fit, $\Sigma(\log(x_i) - \log(f_i))^2$, where x is a data point and f is its fit value. We find $\Sigma = 0.1$ (M), 0.3 (E), 0.5 (T), 0.07 (D), and 0.07 (R). But it should be kept in mind that the

Author's personal copy

Table 1
Fits to electron energy spectra near the five satellites. If energy (E) in MeV is used in the formula with these parameters, the resulting intensity has the units, counts/cm^2 s sr keV. P_leading is computed by integrating Eq. (1) for leading electrons between the resonance energy and 10 MeV. Also, the last column is the integration of Eq. (1) for the range of energies from 30 keV to 10 MeV. The integrated power per unit areas is expressed as eV/cm^2 s.

	j_o	E_o (MeV)	a	b	P_leading	P_total
Mimas	5000	1	0.9	−4.6	1.21×10^{12}	1.81×10^{12}
Enceladus	14,000	1.05	1.2	−7	3.02×10^{11}	8.11×10^{11}
Tethys	50,000	1.05	1.06	−8.9	1.91×10^{11}	1.08×10^{12}
Dione	30,000	1.2	0.5	−11	6.41×10^{10}	7.60×10^{11}
Rhea	22,000	0.21	−0.2	−5.3	8.40×10^{9}	2.94×10^{11}

Table 2
Fit parameters to the proton spectra between 0.1 and 1 MeV for Tethys, Dione, and Rhea and integrated power per unit area for this energy range (eV/cm^2 s). The fit function used is $j=A(E/E_T)^n$, where E is in keV and j is in counts per cm^2 s sr keV. For Mimas and Enceladus, we fit the CRAND peak by dividing the energy interval between 1 and 50 MeV and adding the separate contributions.

	A	E_T (keV)	n	P
Mimas				2.0×10^{8}
Enceladus				3.7×10^{7}
Tethys	6.0	213.0	−3.3	1.7×10^{9}
Dione	20.0	180.0	−3.35	3.2×10^{9}
Rhea	200.0	102.0	−3.9	3.5×10^{9}

integrated quantities are approximations. The coverage of the energy range of interest by the LEMMS instrument channels is very coarse.

In Table 1, we also include an integration of Eq. (1) done in two different ways. In the first integration, we begin at the electron resonance energy appropriate to the satellite in question and integrate to 10 MeV; this gives the approximate energy into the leading hemisphere from energetic electrons. For comparison, in the second integration, we use the energy limits 30 keV to 10 MeV at all the satellites. The table shows that the leading energy input maximizes at Mimas and is a falling function with increasing radial distance. This is consistent with the conjecture in Schenk et al. (2011).

For the moment of the distribution function presented by Eq. (1), the power per unit area is likely to be dominated by the energetic plasma. To confirm this we integrated the Rhea spectrum down to 100 eV assuming it as a reasonable approximation to extrapolate the fit to low energies. We find this adds about 15% to the power per unit area at Rhea. Therefore, we hypothesize that the power per unit area is dominated by energetic electrons. These deposit their energy much deeper into the ice than incident cold electrons or energetic ions. In assessing the nature of the electron weathering on the surface reflectance spectra (e.g. where the ice might be brightening in a specific range of wavelengths), the penetration depth of the relevant charged particles must be compared to the range of depths at which photons are reflected from the surface.

Next we consider protons. At radiation belt energies, there is also an evidence of significant weathering in the macrosignatures of Mimas and Enceladus. Krupp et al. (2009) have shown the large flux differences inside the sweeping corridors of the moons and just outside of them. For our work here we will use the fluxes inside the sweeping corridors of Mimas and Enceladus, because of the large radial variations in flux. For the other three moons, we use the average fluxes near their orbits.

In the ring-current range of energies, there is evidence that some ions are nearly absent due to rapid CE with the neutrals and absorption by the bodies at larger distances. ENA imaging shows that tens to hundreds of keV protons are not present in large numbers inside of about Dione's orbit. The shape of proton energy spectra also suggests that the hundreds of keV energies are not fully populated. This likely means that there is an important weathering component missing, except possibly at Rhea. We have not fully explored energetic heavy ions here partly due to measurement limitations. Dialynas et al. (2009) have begun the process of describing the radial dependence of energetic oxygen spectra from the Cassini data.

To quantify these effects further and compare the ring-current and radiation belt energies, we fit the proton spectra displayed in Fig. 4. For the three outer moons, we fit power-law spectra in the energy range between about 100 keV and 1 MeV and compute the power using Eq. (1), see Table 2 for details. We do not compute this power for the two inner moons because penetrating background in the energy channels at these distances is a problem. Among the three outer moons in our study, the fluxes are comparable. In Table 2, we also present an estimate of the power from the CRAND peak. To estimate this power, we divided up the 1–50 MeV energy range and used an interpolation between data points at each energy to perform a sum that approximates the area under the peak.

5. Summary

We have considered several-year average charged particle data obtained in Saturn's inner magnetosphere. Using these averages, we have also computed energy spectra near five of Saturn's satellites and integrated to find power per unit area into the surface. Our goal has been to compare the particle environments near these satellites to make predictions about their contributions to the weathering of these icy bodies. We have shown that all five satellites receive most of their electron power from energetic particles. Energetic electrons whose net motion is retrograde relative to the icy satellites deposit the most power per unit area into Mimas's surface. This is consistent with the correlation to features obtained by optical remote sensing that was reported in Schenk et al. (2011). In that paper, slightly less intense electron energy spectra were used near Mimas and Tethys.

If we restrict ourselves to fluxes within the moon sweeping corridors of Mimas and Enceladus, we find an important contribution to weathering from the CRAND peak. But because we are working with different energy ranges in these estimates, it is not appropriate for instance to compare the ion and electron levels. The steep proton power-law behavior below the CRAND energy range is likely due to the replacement of energetic ions by lower energy pick-up ions in CE with the dense neutral cloud. Hence these particles play a much smaller role in modifying the surfaces of the inner satellites.

References

Armstrong, T.P., Taherion, S., Manweiler, J., Krimigis, S.M., Paranicas, C., Mitchell, D., Krupp, N., 2009. Energetic ions trapped in Saturn's inner magnetosphere. Planet. Space Sci. 57, 1723–1731.

Buratti, B.J., Mosher, J.A., Nicholson, P.D., McGhee, C.A., French, R.G., 1998. Near-infrared photometry of the Saturnian satellites during ring plane crossing. Icarus 136, 223–231.

Carbary, J.F., Mitchell, D.G., Krupp, N., Krimigis, S.M., 2009. L shell distribution of energetic electrons at Saturn. J. Geophys. Res. 114, A09210. doi:10.1029/2009JA014341.

Carbary, J.F., Mitchell, D.G., Brandt, P., Roelof, E.C., Krimigis, S.M., 2008. Statistical morphology of ENA emissions at Saturn. J. Geophys. Res. 113, A05210. doi:10.1029/2007JA0128873.

Carlson, R.W., et al., 2009. Europa's surface composition. In: Pappalardo, R.T., McKinnon, W.B., Khurana, K.K., (Eds.), Europa, pp. 283–327.

Cooper, J.F., 1983. Nuclear cascades in Saturn's rings—Cosmic ray albedo neutron decay and the origins of trapped protons in the inner magnetosphere. J. Geophys. Res. 88, 3945–3954.

Author's personal copy

Dialynas, K., Krimigis, S.M., Mitchell, D.G., Hamilton, D.C., Krupp, N., Brandt, P.C., 2009. Energetic ion spectral characteristics in the Saturnian magnetosphere using Cassini/MIMI measurements. J. Geophys. Res., 114. doi:10.1029/2008JA013761.

Hamilton, D., Burns, J., 1994. Origin of Saturn's E-ring: self-sustained, naturally. Science 264, 550–553.

Johnson, R.E., Carlson, R.W., Cooper, J.F., Paranicas, C., Moore, M.H., Wong, M.C., 2004. Radiation effects on the surfaces of the Galilean satellites. In: Bagenal, F., Dowling, T., McKinnon, W. (Eds.), Jupiter: The Planet, Satellites and Magnetosphere. Cambridge University Press, Cambridge, pp. 485–512.

Johnson, R.E., 1990. Energetic Charged Particle Interactions with Atmospheres and Surfaces. Springer-Verlag, Berlin.

Johnson, R.E., 1985. Polar frost on Ganymede. Icarus 62, 344–347.

Kollmann, P., et al. Energetic particle phase space densities at Saturn: observations and interpretations, J. Geophys. Res., in press, doi:10.1029/2010JA016221.

Krimigis, S.M., et al., 2004. Magnetosphere imaging instrument (MIMI) on the Cassini mission to Saturn/Titan. Space Sci. Rev. 114, 233–329.

Krupp, N., et al. (2009), Energetic particles in Saturn's magnetosphere during the Cassini nominal mission (July 2004–July 2008), Planet. Space Sci., 10.1016/j.pss.2009.06.010.

Mauk, B.H., Fox, N., 2010. Electron radiation belts of the Solar System, J. Geophys. Res., 115, A12220, doi:10.1029/2010JA015660.

McEntire, R.W., Mitchell, D.G., 1989. Instrumentation for global magnetospheric imaging via energetic neutral atoms. In: Waite Jr., J.H., Burch, J.L., Moore, R.L. (Eds.), Solar System Plasma Physics. AGU, Washington, DC, pp. 69–80.

McEwen, A.S., 1986. Exogenic and endogenic albedo and color patterns on Europa. J. Geophys. Res. 91, 8077–8097.

Paranicas, C., et al., 2010. Transport of energetic electrons into Saturn's inner magnetosphere. J. Geophys. Res. 115, A09214. doi:10.1029/2010JA015853.

Paranicas, C., et al., 2008. Sources and losses of energetic protons in Saturn's magnetosphere. Icarus 197, 519–525.

Paranicas, C., Carlson, R.W., Johnson, R.E., 2001. Electron bombardment of Europa. Geophys. Res. Lett. 28, 673–676.

Pospieszalska, M.K., Johnson, R.E., 1989. Magnetospheric ion bombardment profiles of satellites: Europa and Dione. Icarus 78, 1–13.

Roussos, E., et al., 2011. Long and short term variability of Saturn's ionic radiation belts, J. Geophys. Res., 116, A02217, doi:10.1029/2010JA015954.

Roussos, E., et al., 2008. Discovery of a transient radiation belt at Saturn. Geophys. Res. Lett., 35. doi:10.1029/2008GL035767.

Schenk, P., Hamilton, D.P., Johnson, R.E., McKinnon, W.B., Paranicas, C., Schmidt, J., Showalter, M.R., 2011. Plasma, plumes and rings: Saturn system dynamics as recorded in global color patterns on its midsize satellites. Icarus 211, 740–757.

Schulz, M., Lanzerotti, L.J., 1974. Particle Diffusion in the Radiation Belts. Springer-Verlag, Berlin.

Sullivan, J.D., 1971. Geometrical factor and directional response of single and multi-element particle telescopes. Nucl. Instr. and Meth. 95, 5–11.

Thomsen, M., Van Allen, J.A., 1980. Motion of trapped electrons and protons in Saturn's inner magnetosphere. J. Geophys. Res. 85, 5831–5834.

Williams, D.J., Mauk, B.H., McEntire, R.W., 1998. Properties of Ganymede's magnetosphere as revealed by energetic particle observations. J. Geophys. Res. 103, 17,523–17,534.